Finite Difference Formulation

The central difference formulation is used for grid points inside the domain. Thus, the finite difference equations for grid point (i,j) are

$$u_{i,j}^{n-1}\frac{\bar{\delta}_x u_{i,j}^n}{2\Delta x}+v_{i,j}^{n-1}\frac{\bar{\delta}_y u_{i,j}^n}{2\Delta y}+\frac{\bar{\delta}_x P_{i,j}^n}{2\Delta x}-Re^{-1}\left[\frac{\bar{\delta}_x^2 u_{i,j}^n}{\Delta x^2}+\frac{\bar{\delta}_y^2 u_{i,j}^n}{\Delta y^2}\right]=0 \tag{12}$$

$$u_{i,j}^{n-1}\frac{\bar{\delta}_x v_{i,j}^n}{2\Delta x}+v_{i,j}^{n-1}\frac{\bar{\delta}_y v_{i,j}^n}{2\Delta y}+\frac{\bar{\delta}_y P_{i,j}^n}{2\Delta y}-Re^{-1}\left[\frac{\bar{\delta}_x^2 v_{i,j}^n}{\Delta x^2}+\frac{\bar{\delta}_y^2 v_{i,j}^n}{\Delta y^2}\right]=0 \tag{13}$$

$$\frac{\bar{\delta}_x u_{i,j}^n}{2\Delta x}+\frac{\bar{\delta}_y v_{i,j}^n}{2\Delta y}=0 \tag{14}$$

where

$$\bar{\delta}_x q_{i,j}=q_{1+1,j}-q_{1-1,j} \tag{15}$$

$$\bar{\delta}_y q_{i,j}=q_{1,j+1}-q_{1,j-1} \tag{16}$$

$$\delta_x^2 q_{i,j}=q_{1+1,j}-2q_{i,j}+q_{1-1,j} \tag{17}$$

$$\delta_y^2 q_{i,j}=q_{1,j+1}-2q_{i,j}+q_{1,j-1} \tag{18}$$

The Neumann boundary conditions for the normal component of velocity at the wall can be satisfied automatically if we apply the finite difference equations for the momentum equations to grid points on boundaries where both Dirichlet and Neumann boundary conditions exist. For instance, for horizontal wall boundaries, we have $u=0$, $v=0$, and $\partial v/\partial y=0$. Thus, Eq. (13) becomes

$$\frac{\Delta P_{i,j}^n}{\Delta y}+Re^{-1}\left[\frac{2\Delta v_{i,j}^n}{\Delta y^2}\right]=0 \tag{19}$$

The Dirichlet boundary condition $v=0$ is used to replace the continuity equation. In this way, both Dirichlet and Neumann boundary conditions are implemented with the continuity equation satisfied. For grid points inside the flow region, Eqs. (12–14) are implemented and for grid points on the wall boundaries, the momentum equations take the form of Eq. (19). These equations are solved simultaneously while the nonlinear system is updated by Newton-Raphson method. With the boundary condition switching, staggered grids are not necessary and there is no pressure oscillation found.

Results and Discussions

The first test flow problem is the incompressible laminar flow between concentric rotating cylinders. The exact solution can be found in textbooks on fluid mechanics (see, e.g., Schlichting[5]). Numerical solutions for this problem can be compared with the exact solution to estimate the accuracy. In this test case, the inner cylinder with radius r_1 is stationary and the outer cylinder with radius r_2 rotates with angular velocity ω. The dimensionless primitive variable form of the Navier-Stokes equations in polar coordinates is solved. Velocity components are nondimensionalized with respect to the outer cylinder tangential velocity $r_2\omega$. All lengths are nondimensionalized with respect to the inner radius r_1. The dimensionless pressure is defined by $P/\rho(r_2\omega)^2$ and the radius ratio r_2/r_1 is fixed at 2. In this problem, a 10×16 mesh is employed. Both FEM and FDM are applied on the same grid. Numerical results obtained by both methods are very close to each other. Numerical results show that the dimensionless solutions of this problem are independent of Reynolds number. In Fig. 1, tangential velocity distribution is shown as a function of r/r_1. The relative pressure $P-P_i$ is also plotted in Fig. 1. Good agreement between our numerical results and the analytical solution can be seen.

The second flow problem solved with the present method is the flow in a duct with the sudden enlargement. The definition of the flowfield geometry is $1.5H$ at the duct inlet and $2.5H$ at the duct exit with a back-step heigh H. The length of the duct from the back step to duct exit is $20H$ and the length from duct inlet to the back step is $9H$. The computation was performed for Reynolds numbers of 200, 400, and 1000 on a grid with 2169 grid points. The present method is implemented on the same grid with both FEM and FDM. The dimensionless pressure $P/[(\rho_\infty V_\infty^2)/2]$ contours are shown in Fig. 2. Pressure values change continually and smoothly along the duct. There is no spurious pressure value observed. Thus, the pressure-filtering procedure is not needed. Velocity fields in the region close to the back step are shown in Fig. 3. At the duct inlet and the duct exit, velocity profiles present fully developed laminar flows. Near the back step a circulation zone is observed. For higher Reynolds number the reattachment point moves further downstream.

Acknowledgment

This work was supported by the National Sciences and Engineering Research Council of Canada.

References

[1]Peeters, M. F., Habashi, W. G., and Dueck, E. G., "Finite-Element Stream Function-Vorticity Solutions of the Incompressible Navier-Stokes Equations," *International Journal for Numerical Methods in Fluids,* Vol. 7, No. 4, 1987, pp. 17–27.

[2]Habashi, W., Peeters, M., Guevremont, G., and Hafes, M., "Finite-Element Solutions of the Compressible Navier-Stokes Equations," *AIAA Journal,* Vol. 25, No. 7, 1987, pp. 944–948.

[3]Sani, R. L., Gresho, P. M., Lee, R. L., and Griffiths, D. F., "The Cause and Cure (?) of the Spurious Pressure Generated by Certain FEM Solutions of the Incompressible Navier-Stokes Equations: Pt. 1," *International Journal for Numerical Methods in Fluids,* Vol. 1, No. 1, 1981, pp. 17–43.

[4]Strikwerda, J. C., "Finite-Difference Methods for the Stokes and Navier-Stokes Equations," *SIAM Journal on Scientific and Statistical Computing,* Vol. 5, No. 1, 1984, pp. 56–68.

[5]Schlichting, H., *Boundary-Layer Theory,* McGraw-Hill, New York, 1968, Chap. 5.

Forebody Vortex Control with the Unsteady Bleed Technique

D. R. Williams* and H. Papazian†
Illinois Institute of Technology, Chicago, Illinois 60616

I. Introduction

THE asymmetric system of vortices that separate from the forebodies of aircraft and missiles at high angles of attack has long been recognized as a significant contributor to the aerodynamic loading on the vehicle.[1–3] Strong yaw moments are created that can overwhelm the control surfaces causing the vehicle to lose control. For example, the unpredictable trajectories of missiles launched at high angles of attack are related to the forces generated by the forebody vortices.

Received March 19, 1990; revision received May 9, 1990; accepted for publication May 9, 1990.

*Associate Professor, Fluid Dynamics Research Center. Member AIAA.

†Former Graduate Research Assistant, Fluid Dynamics Research Center.

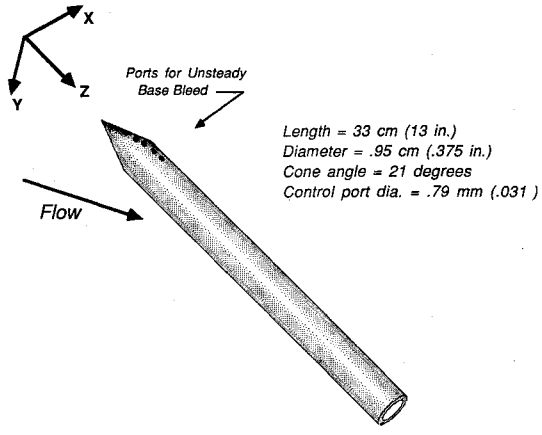

Fig. 1 Schematic of the model showing the location of the unsteady bleed holes.

The asymmetric vortices can be made symmetric or their effects counteracted with external appendages such as strakes and fins. However, there is a penalty of increased drag, and the angle of attack over which these devices are effective is limited. The unsteady base bleed technique is a new method that can control the formation of the Karman vortex street behind a right circular cylinder[4] without the use of external appendages. In this Note, it is shown that the unsteady base bleed can also be used to change the asymmetric flow around a cone-cylinder model at high angles of attack to a symmetric state.

II. Experimental Procedure

All of the tests were conducted in an open return wind tunnel with a cross section of 40 × 61 cm. The freestream velocity was U_o = 3.08 m/s with a freestream turbulence level of 0.25%. The model representing the forebody was a cone-cylinder combination shown in Fig. 1. The cone had a 21-deg included angle and a length of 2.54 cm. The cylinder was 30-cm long with a diameter D = 0.953 cm. The model was hollow and was mounted on a support that allowed it to be set at angles of attack ranging from 0 to 90 deg. The Reynolds number based on the cylinder diameter was 2.1 × 10^3. The velocity measurements were obtained with a laser anemometer and were corrected for biasing with the particle residence-time weighting correction.

The coordinate system was oriented with the origin at the tip of the cone and the positive z coordinate along the model axis. The x coordinate was perpendicular to the body and in the downstream direction. The y axis was across the flow and normal to the centerline of the model.

Flow visualization studies used the smoke-wire technique with illumination from either a strobe light or a copper vapor laser. The strobe light provided a global view of the flowfield. A combination of lenses was used to form the laser beam into a thin sheet of light to obtain detailed cross-sectional views. Two smoke wires were used so that smoke would be entrained into the shear layers on both sides of the model, which was necessary to determine the geometry of the vortices.

The control technique used in this experiment is referred to as unsteady base bleed because a small amount of air was periodically pumped in and out of the model in the base region. The forcing system was completely closed except for the four small base bleed holes (d_j = 0.79-mm diam) on the back of the model, as shown in Fig. 1. On average, over the forcing cycle there was no net mass addition. Placing two bleed holes on the cylinder and two at the base of the cone produced the largest change in the flow for a given forcing amplitude. A B&K Instruments vibration exciter was powered by a 60-W Dynaco power amplifier and Hewlett-Packard function generator. The vibration exciter drove two diaphragm-type chambers. The rms velocity fluctuation level V' at the exit of the unsteady bleed holes was measured with a hot-wire anemometer.

A previous study[4] of the unsteady bleed technique showed that the mean flow was modified primarily by momentum addition. Increasing the rms velocity level or increasing the size of the unsteady bleed holes resulted in a larger change in the flow. The strength of the unsteady bleed effect can be represented as the ratio of the momentum flux from the unsteady bleed ports to the momentum flux of the freestream flow. This ratio is the unsteady bleed coefficient,

$$C_b = (n_j d_j^2 V'^2)/(D^2 U_o^2)$$

where n_j is the number of unsteady bleed holes. In this experiment, C_b was varied from 0.013 to 0.227.

When C_b was maintained at a constant level, the effect on the forebody vortices was found to be independent of frequency, at least over the range of St = 0.4–0.63. Here, St = fD/U_o, where f is the forcing frequency. For this study, St = 0.2 because it allowed the largest variation in C_b.

III. Results

A comparison of the flow around the forebody at a 55 deg angle of attack with and without unsteady base bleed is shown in Figs. 2. Shown in Fig. 2a is the unforced case where the ac-

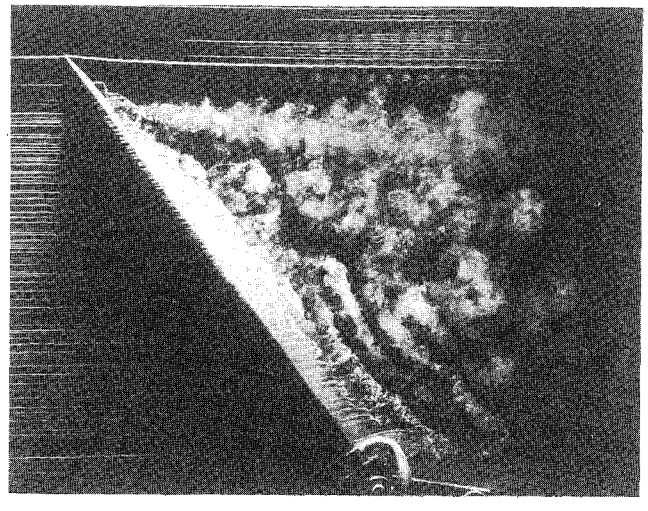

Fig. 2a Flow around the forebody model at 55 deg angle of attack without flow control.

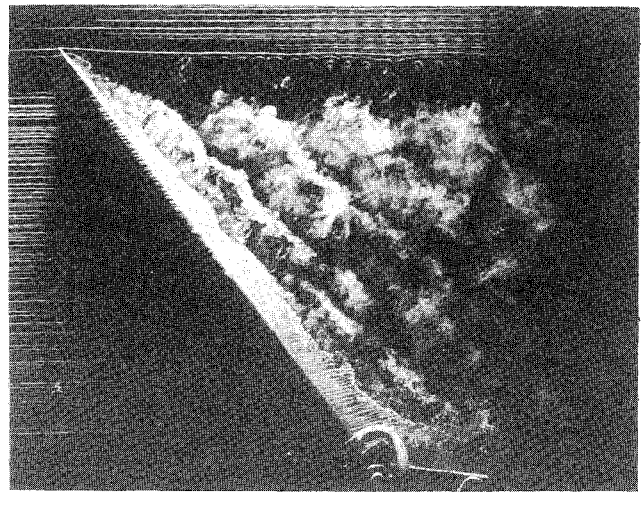

Fig. 2b Unsteady base bleed activated at St = 0.2 and C_b = 0.146.

cumulation of smoke into the first vortex (tip vortex) was evident. The vortex began to form along the base region of the cone, then separated at approximately $x/D = 6$. The tip vortex was steady at this location, although the flow below it was shedding in an unsteady manner, analogous to the Karman vortex street. In Fig. 2b, the unsteady base bleed was activated to control the flow with $St = 0.2$ and $C_b = 0.146$. The strong stationary vortex was no longer present, and the region of unsteady shedding vortices moved closer to the tip of the model from $z/D = 7$ to 4.

To obtain more detailed information about the structure of the flow, a laser light sheet was positioned perpendicular to the axis of the cylinder at $z/D = 4$ from the tip. The views looking down the axis of the model in Figs. 3 show the dependence of the flowfield on increasing forcing amplitude where C_b was varied from 0 to 0.284. The unforced case is shown in Fig. 3a. The strong asymmetry in the smoke pattern was a result of the vortex on the right side of the model. Figures 3b–d correspond to $C_b = 0.03$, 0.146, and 0.284, respectively. The vortex became more diffuse and the streaklines were more symmetric as C_b was increased. The control effect appeared to change continuously as the forcing amplitude was increased. Smaller vortices still appeared in the flow visualization in Fig. 3d, but their presence did not produce a detectable asymmetry in the velocity contours.

Since flow visualization is potentially misleading, the effects of forcing were studied with quantitative velocity measurements. The u-velocity component was measured in the same plane as the laser light sheet flow visualization photographs, where u is the velocity component perpendicular to the cylinder axis. The mean flow data are shown in Figs. 4 in the form of contour maps of constant velocity in the x,y plane.

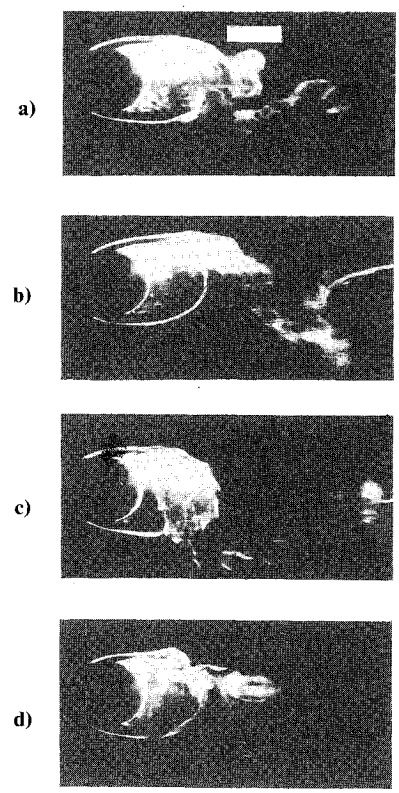

Fig. 3 Flow visualization with light sheet at $z/D = 4$: a) no forcing; b) $C_b = 0.030$; c) $C_b = 0.146$; d) $C_b = 0.284$.

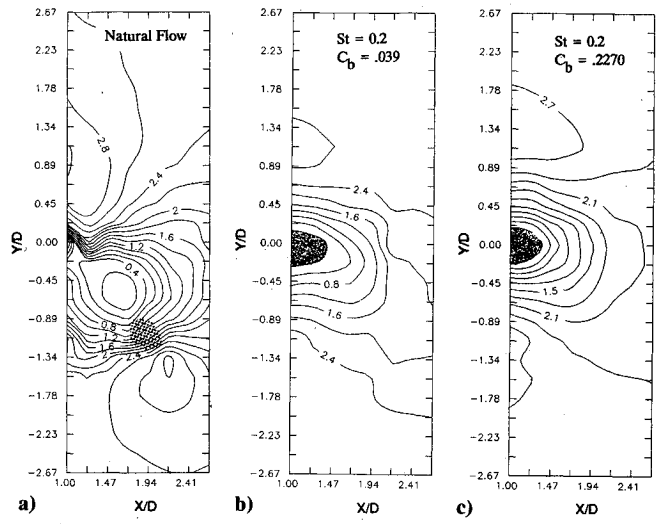

Fig. 4 Contours of constant u velocity in the x,y plane at $z/D = 4$. Contour labels indicate speed in meters per second. Reverse flow regions have been shaded: a) no forcing, tip vortex indicated by dotted region; b) $C_b = 0.039$; c) $C_b = 0.227$.

The measurements were taken at six x locations ranging from $1.0 < x/D < 2.5$ and at 15 y locations from $-2.7 < y/D < 2.7$. The position $y/D = 0$ was directly behind the cylinder.

In the naturally occurring flow, shown in Fig. 4a, the lowest velocity region occurred off center at $y/D = -0.5$ and $x/D = 1.5$. The position of the vortex coincided with the maximum in the shear component $\partial u/\partial y = 430 s^{-1}$, which is shown as the dotted region located at $x/D = 1.9$ and $y/D = -1.0$. This location corresponded to the position of the vortex in the flow visualization (Fig. 3a). In the cases where the control was activated, the flow became more symmetric as the bleed coefficient was increased from 0.4 (Fig. 4b) to 0.227 (Fig. 4c), and a recirculation region formed behind the cylinder, which is indicated by the shaded regions. Therefore, the quantitative measurements confirmed the observations made with the smoke wire flow visualization; namely, the strong tip vortex was eliminated. Additional flow visualization studies indicated that the unsteady base bleed was an effective flow control technique over the range of 30- to 60-deg angle of attack. The results showed that the asymmetric vortices and flowfield could be reduced to a symmetric state without using external appendages.

Acknowledgments

This investigation was conducted with the support of the Air Force Office of Scientific Research under Contract F49620-86-C-0133, monitored by H. Helin and J. McMichael.

References

[1]Ericsson, L. E., and Reding, J. P., "Steady and Unsteady Vortex-Induced Asymmetric Loads on Slender Vehicles," *Journal of Spacecraft and Rockets,* Vol. 18, No. 2, 1980, pp. 97–109.

[2]Thomson, K. D., and Morrison, D. F., "The Spacing, Position, and Strength of Vortices in the Wake of Slender Cylindrical Bodies at Large Incidence," *Journal of Fluid Mechanics,* Vol. 50, Pt. 4, 1971, pp. 751–783.

[3]Ericsson, L. E., and Reding, J. P., "Dynamics of Forebody Flow Separation and Associated Vortices," *Journal of Aircraft,* Vol. 22, No. 4, 1985, pp. 329–335.

[4]Williams, D. R., and Amato, C. W., "Unsteady Pulsing of Cylinder Wakes," *Frontiers in Experimental Fluid Mechanics,* edited by M. Gad-el-Hak, Lecture Notes in Engineering, Vol. 46, Springer-Verlag, Berlin, 1989, pp. 337–364.